

Intrinsically Low Thermal Conductivity in BiSbSe₃: A Promising Thermoelectric Material with Multiple Conduction Bands

Xiaoying Liu, Dongyang Wang, Haijun Wu,* Jinfeng Wang, Yang Zhang, Guangtao Wang, Stephen J. Pennycook, and Li-Dong Zhao*

Bi₂Se₃, as a Te-free alternative of room-temperature state-of-the-art thermoelectric (TE) Bi₂Te₃, has attracted little attention due to its poor electrical transport properties and high thermal conductivity. Interestingly, BiSbSe₃, a product of alloying 50% Sb on Bi sites, shows outstanding electron and phonon transports. BiSbSe₃ possesses orthorhombic structure and exhibits multiple conduction bands, which can be activated when the carrier density is increased as high as $\approx 3.7 \times 10^{20} \text{ cm}^{-3}$ through heavily Br doping, resulting in simultaneously enhancing the electrical conductivities and Seebeck coefficients. Meanwhile, an extremely low thermal conductivity ($\approx 0.6\text{--}0.4 \text{ W m}^{-1} \text{ K}^{-1}$ at 300–800 K) is found in BiSbSe₃. Both first-principles calculations and elastic properties measurements show the strong anharmonicity and support the ultra-low thermal conductivity of BiSbSe₃. Finally, a maximum dimensionless figure of merit $ZT \sim 1.4$ at 800 K is achieved in BiSb(Se_{0.94}Br_{0.06})₃, which is comparable to the most *n*-type Te-free TE materials. The present results indicate that BiSbSe₃ is a new and a robust candidate for TE power generation in medium-temperature range.

by the dimensionless figure of merit ZT defined as $ZT = (S^2\sigma/\kappa) T$, where S , σ , κ , and T denote the Seebeck coefficient, electrical conductivity, thermal conductivity, and working temperature in Kelvin, respectively. An efficient TE material needs high power factor ($PF = S^2\sigma$) and low thermal conductivity (κ). However, the complex interrelation among these parameters makes it difficult to improve the overall efficiency. To date, many emerging methods have been effectively employed to optimize final ZT s, including enhancing power factor through modifying electronic band structures,^[8–11] reducing lattice thermal conductivity through designing nanostructures,^[12–14] or all-length-scale hierarchical architectures.^[15] Alternatively, one can seek promising candidates, which intrinsically possess more than one of the main ingredients of good TE materials,^[16–19] such as a large Seebeck coefficient, high electrical conductivity, or low thermal conductivity.

1. Introduction

Thermoelectric (TE) technology that can directly and reversibly convert heat to electrical energy has received wide attention due to global energy and environmental demands.^[1–7] But the application of TE technology is limited by the low power generation conversion efficiency which is determined

beck coefficient, high electrical conductivity, or low thermal conductivity.

As one narrow bandgap semiconductor, Bi₂Te₃ possesses excellent electrical conductivity and Seebeck coefficient, and thus it is one of classic room-temperature TE materials. ZT s for both *n*-type and *p*-type Bi₂Te₃-based systems are larger than unity, which have been widely applied for TE power generation and electronic cooling around room temperature for several decades.^[20,21] It is well known that Te is a scarce element in the crust of the earth, additionally, the cost of Te would rise sharply along with the Te-containing TE materials reach mass markets. A broad search for inexpensive alternatives is therefore warranted. In this case, the Te-free TE materials have attracted huge interest. As a sister compound of Bi₂Te₃, Bi₂Se₃ has drawn little attention due to its inferior TE performance ($ZT \sim 0.4$).^[21,22] The key factors that limit the ZT s of Bi₂Se₃ are its poor electrical transport properties and high thermal conductivity.^[21,23]

In this work, to improve the TE performance of Bi₂Se₃, we introduced Sb substitutions on Bi sites. Interestingly, BiSbSe₃ has extremely low thermal conductivity $\approx 0.40\text{--}0.60 \text{ W m}^{-1} \text{ K}^{-1}$ at 300–800 K, which is related to the phase transition from the rhombohedral structure of Bi₂Se₃ to the orthorhombic structure of Sb₂Se₃. Therefore, it is expected that BiSbSe₃ could display a promising TE performance after optimizing carrier density via

X. Liu, D. Wang, Prof. L.-D. Zhao
School of Materials Science and Engineering
Beihang University
Beijing 100191, China
E-mail: zhaolidong@buaa.edu.cn

H. Wu, Y. Zhang, Prof. S. J. Pennycook
Department of Materials Science and Engineering
National University of Singapore
Singapore 117575, Singapore
E-mail: wu.haijun@u.nus.edu

Prof. J. Wang, Prof. G. Wang
College of Physics and Materials Science
Henan Normal University
Xinxiang 453007, China

 The ORCID identification number(s) for the author(s) of this article can be found under <https://doi.org/10.1002/adfm.201806558>.

DOI: 10.1002/adfm.201806558

electrons doping. Meanwhile, we aimed at investigating the origins of the low thermal conductivity of BiSbSe_3 , and found that BiSbSe_3 possesses very low elastic properties (phonon velocity v_a , Young's modulus E) and large Grüneisen parameter γ , which are related to its **strong anharmonicity caused by lone-pair electrons come from Sb/Bi in BiSbSe_3** . These experimental results are well supported by theoretical calculations on phonon dispersions. Additionally, the multiple conduction bands of BiSbSe_3 imply a possibility to improve the electrical transport properties (power factor) by manipulating these bands through introducing a higher density of electron carriers. Our results show that the carrier density can be increased to as high as $\approx 3.7 \times 10^{20} \text{ cm}^{-3}$ through Br doping, which could activate Fermi electron pockets and enhance Seebeck coefficients. Finally, we obtained a $ZT \sim 1.4$ at 800 K due to enhanced power factor ($\approx 7.4 \mu\text{W cm}^{-1} \text{ K}^{-2}$) and favorable thermal conductivity ($\approx 0.43 \text{ W m}^{-1} \text{ K}^{-1}$), the superior performance of BiSbSe_3 is competing with most of the state-of-the-art medium-temperature n -type TE materials, such as Bi_2Se_3 ($ZT \sim 0.4$ at 600 K), $\text{Bi}_2(\text{Te,Se})_3$ ($ZT \sim 1.0$ at 400 K),^[24] SnSe polycrystalline ($ZT \sim 1.2$ at 800 K),^[25] PbS ($ZT \sim 0.9$ at 800 K),^[26] Bi_2S_3 ($ZT \sim 0.6$ at 760 K),^[27] etc.

2. Results and Discussions

In this work, we first optimized the Bi substitution by Sb which can induce the phase transition and selected the best Sb substitution fractions based on TE transport properties, and

then optimized its electrical transport properties through Br doping. The X-ray diffraction patterns of $\text{Bi}_{2-x}\text{Sb}_x\text{Se}_3$ shows a rhombohedral structure for Bi_2Se_3 and $\text{Bi}_{1.5}\text{Sb}_{0.5}\text{Se}_3$ samples, while the samples of BiSbSe_3 , $\text{Bi}_{0.5}\text{Sb}_{1.5}\text{Se}_3$, and Sb_2Se_3 show an orthorhombic structure, as shown in Figure S1a in the Supporting Information. For $x = 0.02$ – 0.08 , all samples display a single phase without noticeable impurities, as shown in Figure S1b in the Supporting Information. There is a clear evidence of an additional phase for $x = 0.10$ ($\text{Bi}_3\text{Se}_4\text{Br}$), revealing the solubility limit of Br in BiSbSe_3 . To clearly confirm the structure of (Br-doped) BiSbSe_3 , compared with the two end terminal members of Bi_2Se_3 and Sb_2Se_3 , we employed electron diffraction and scanning transmission electron microscopy (STEM) imaging techniques.^[28] The Bi_2Se_3 exhibits five-layer structure ($-\text{Se}^{(1)}-\text{Bi}-\text{Se}^{(2)}-\text{Bi}-\text{Se}^{(1)}-$) as Bi_2Te_3 ,^[29] as shown in Figure 1a,b. Through 50% alloying with Sb on Bi site, the BiSbSe_3 totally changes to the structure of Sb_2Se_3 without any precipitates. Figure 1c–h shows the representative electron diffraction patterns of (Br-doped) BiSbSe_3 along [100], [010], and [011] zone axes, respectively. The experimental patterns are well consistent with the simulated patterns of Sb_2Se_3 . The respective atomically resolved STEM high-angle annular dark-field (HAADF) images in Figure 1d,f,h show that the structure is spring-like with zigzag atom arrangements, which is similar to that of SnSe ,^[16] while quite different from the straight layers of Bi_2Se_3 . The spring-like structure exhibits anharmonic and anisotropic bonds, hinting a high anharmonicity for intrinsically low lattice thermal conductivities.

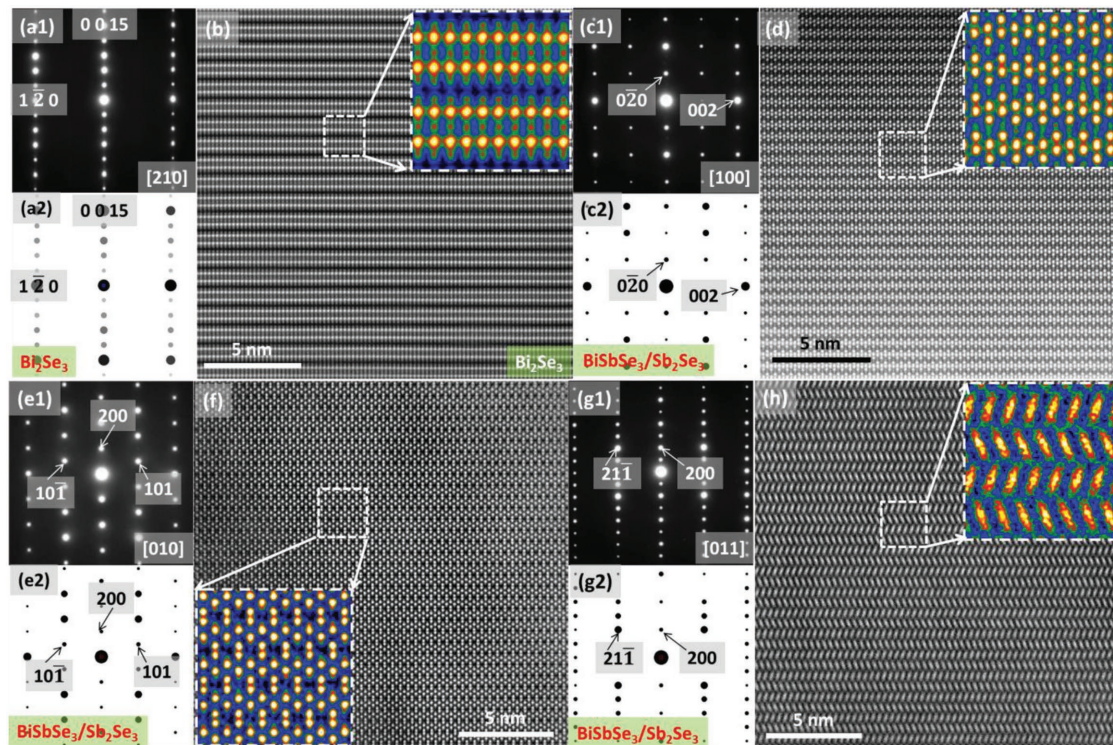


Figure 1. Structural characterizations of BiSbSe_3 , and comparisons with two terminal compounds of Bi_2Se_3 and Sb_2Se_3 . a1,a2) Experimental and simulated electron diffraction patterns of Bi_2Se_3 along [210] zone axis. b) Atomically resolved STEM HAADF image of Bi_2Se_3 along [210] zone axis, with enlarged image inset. c1,c2,e1,e2,g1,g2) Experimental and simulated electron diffraction patterns along [100], [010], and [011] zone axes. d,f,h) Atomically resolved STEM HAADF images of BiSbSe_3 or Sb_2Se_3 along [100], [010], and [011] zone axes, with enlarged images insets.

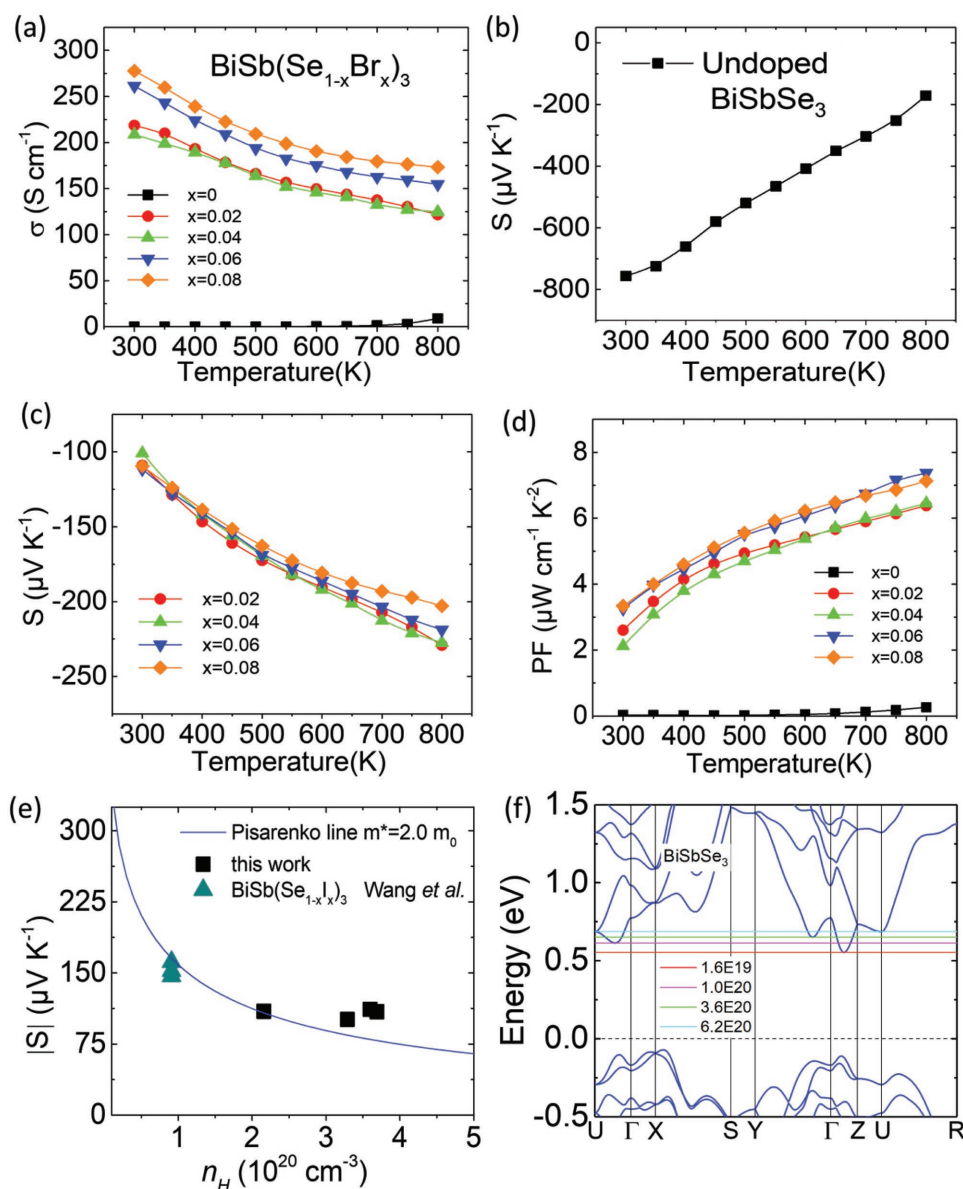


Figure 2. TE transport properties as a function of temperature for $\text{BiSb}(\text{Se}_{1-x}\text{Br}_x)_3$ with different Br doping fractions x ($x = 0-0.08$) and calculated band structures: a) electrical conductivity; b) and c) Seebeck coefficient; d) power factor; and e) calculated Pisarenko line of BiSbSe_3 ($m^* \sim 2.0m_0$) by using the single parabolic model at 300 K. The experimental Seebeck coefficients (black spots) deviate to the theoretical line with increasing carrier density, suggest the contribution of the multiple conduction bands of BiSbSe_3 . The experimental Seebeck coefficients from the BiSbSe_3 ^[31] fall in the Pisarenko line. Calculated band structures f) BiSbSe_3 in which the Fermi levels were set to zero. The horizontal lines in f) refer to the carrier densities (in cm^{-3}) and the corresponding chemical potentials at room temperature.

To further investigate the characteristics of BiSbSe_3 , we measured the bandgap of $\text{Bi}_{2-x}\text{Sb}_x\text{Se}_3$ as shown in Figure S2 in the Supporting Information. Compared with the narrow bandgap of Bi_2Se_3 (≈ 0.25 eV), BiSbSe_3 shows a larger bandgap of ≈ 0.88 eV, comparable to that of Sb_2Se_3 (≈ 1.17 eV). The first-principles density of functional theory (DFT) calculations were also performed and results are shown in Figure 2 and Figure S3 in the Supporting Information. Considering the two nonequivalent sites of Sb atom in Sb_2Se_3 (Figure S4a, Supporting Information), two possible structures can be formed and the lower energy structure with Sb1 substituted by Bi atom was adopted

to modeling the BiSbSe_3 (Figure S4b, Supporting Information). The calculated bandgaps are ≈ 0.16 , 0.75 , and 0.63 eV for Bi_2Se_3 , Sb_2Se_3 , and BiSbSe_3 , respectively, as shown in Figure 2 and Figure S3 in the Supporting Information. Although the DFT calculations cannot give quantitatively accurate predictions of the bandgap, the trends are more reliable. For Bi_2Se_3 , both the valence band maximum (VBM) and conduction band minimum (CBM) are located at Γ points, while for other two compounds, both the VBM and CBM are along Γ -Z direction, identifying them as direct bandgap semiconductors. The energy difference between CBM and the fourth valence valley is less than

Table 1. Room-temperature carrier density and mobility for BiSb(Se_{1-x}Br_x)₃ ($x = 0-0.08$), indicating Br is an effective dopant that could dramatically enhance carrier density.

Samples	n_H ($\times 10^{19} \text{ cm}^{-3}$)	μ_H [$\text{cm}^2 \text{ V}^{-1} \text{ s}^{-1}$]
BiSbSe ₃	0.0014	23.1
BiSb(Se _{0.98} Br _{0.02}) ₃	21.59	6.33
BiSb(Se _{0.96} Br _{0.04}) ₃	32.89	3.96
BiSb(Se _{0.94} Br _{0.06}) ₃	35.98	4.40
BiSb(Se _{0.92} Br _{0.08}) ₃	36.89	4.57

≈ 0.10 eV, which is smaller than that of ≈ 0.13 eV between the first and third valence bands in SnSe.^[30] Such small energy difference can be easily crossed at elevated temperature, leading to enhancements in electrical transport properties.

After optimizing Sb substitutions by Bi, Figure S5 in the Supporting Information, we found that BiSbSe₃ could exhibit the lowest thermal conductivity as that of Sb₂Se₃, but the low bandgap (Figure S2, Supporting Information) suggests us to optimize its carrier density to enhance the TE performance of BiSbSe₃ via Br doping. Figure 2 shows the temperature dependent electrical transport properties of BiSb(Se_{1-x}Br_x)₃ ($x = 0-0.08$). The undoped BiSbSe₃ has a poor electrical conductivity at room temperature, due to its extremely low carrier density (Table 1). With the increase of temperature, the electrical conductivity (σ) increases for BiSbSe₃ (Figure 2a), while decreases for Br contained samples, which is consistent with heavily doped semiconductor behavior. As the content of Br rises, the room-temperature electrical conductivity significantly increases from undoped BiSbSe₃ to $\approx 219 \text{ S cm}^{-1}$ for the BiSb(Se_{0.98}Br_{0.02})₃, and further to $\approx 278 \text{ S cm}^{-1}$ for the BiSb(Se_{0.92}Br_{0.08})₃, which results from the increase of carrier density (Table 1). The carrier density increases from $\approx 1.4 \times 10^{16}$ to $\approx 2.2 \times 10^{20} \text{ cm}^{-3}$ with only 2% Br doping, indicating Br is an effective dopant to increase the carrier density and the electrical conductivity. Absolute Seebeck coefficients ($|S|$) undergoes a significantly decrease from $\approx 756 \mu\text{V K}^{-1}$ for undoped BiSbSe₃ to $\approx 110 \mu\text{V K}^{-1}$ for Br contained samples at room temperature (Figure 2b,c). It is noted that $|S|$ increases with temperature due to Br doping, which is different from BiSbSe₃. The strengthened electrical conductivities and carrier density with increasing Br doping fractions indicate that electron doping has been successfully achieved in BiSbSe₃.

The significantly increased electrical conductivities and slightly declined Seebeck coefficients result in remarkable enhancements in power factors in the whole temperature range, as shown in Figure 2d. The power factor significantly increases from ≈ 0.03 to $\approx 2.6 \mu\text{W cm}^{-1} \text{ K}^{-2}$ at room temperature due to Br doping. Compared to the experimental carrier densities at room temperature (Table 1), it is clearly shown that BiSbSe₃ exhibits a characteristic of multiple bands transport as discussed before. This result is also validated by the Pisarenko plot, the relationship between carrier concentration and Seebeck coefficient, which shows the enhanced Seebeck coefficients due to activating conduction bands through Br doping, as shown in Figure 2e. The solubility limit of Br in BiSbSe₃ ($\leq 8\%$) is higher than that of I in BiSbSe₃ ($\leq 3\%$) since the carrier

concentration of Br-doped BiSbSe₃ samples is more than three times higher than those of I-doped BiSbSe₃,^[31] which confirms the multiple band conduction in BiSbSe₃. Considering that the energy difference (≈ 0.10 eV) is smaller between CBM and the fourth band valley, the multiple band characteristic (Figure 2f) can be easily achieved through tuning the carrier density (Table 1).

As shown in Figure 3a, the total thermal conductivity κ_{tot} of all samples decreases with increasing temperature. All Br-doped samples display higher κ_{tot} than that of undoped BiSbSe₃, which is the result of higher electronic thermal conductivity κ_{ele} (Figure S5d, Supporting Information), according to Wiedemann–Franz law, $\kappa_{\text{ele}} = L\sigma T$. L is the Lorenz number and can be extracted based on fitting of the respective Seebeck coefficient values to the reduced chemical potential (η).^[32,33] The heat capacity (C_p), thermal diffusivity (D), Lorenz number (L), and electrical thermal conductivity (κ_{ele}) were presented in Figure S6 in the Supporting Information. The lattice thermal conductivity κ_l can be calculated by subtracting the electronic thermal conductivity from the total thermal conductivity and the results are shown in Figure 3a. The room-temperature κ_l decreases from $\approx 0.60 \text{ W m}^{-1} \text{ K}^{-1}$ for undoped BiSbSe₃ to $\approx 0.47 \text{ W m}^{-1} \text{ K}^{-1}$ for BiSb(Se_{0.92}Br_{0.08})₃ as shown in Figure 3a. The reduction of κ_l is ascribed to the enhanced phonon scattering by point defects due to the solid solution of Br atom in the Se sublattice. It is worth mentioning that κ_l of undoped BiSbSe₃ already shows a very low value of $\approx 0.6 \text{ W m}^{-1} \text{ K}^{-1}$ at room temperature, which is comparable to those well-known TE materials with intrinsically low lattice thermal conductivities, e.g., BiCuSeO ($\approx 0.88 \text{ W m}^{-1} \text{ K}^{-1}$),^[34] SnSe ($\approx 0.62 \text{ W m}^{-1} \text{ K}^{-1}$),^[16] AgSbTe₂ ($\approx 0.40 \text{ W m}^{-1} \text{ K}^{-1}$),^[35] K₂Bi₈Se₁₃ ($\approx 0.43 \text{ W m}^{-1} \text{ K}^{-1}$),^[36] as displayed in Figure 3b.

Different from the well-known layered TE material SnSe,^[16] Sb₂Se₃ exhibits a chain-like structure along b axis (Figure S4, Supporting Information), although both of them possess the same space group $Pnma$ (#62). There are five nonequivalent atoms in the Sb₂Se₃ unit cell, including two Sb and three Se atoms. These interchain coupling bonds are weaker than that in intrachain, therefore Bi–Se (Sb–Se) bonds could be relatively weaker. To understand the bonding characteristic of BiSbSe₃, the electron localization function (ELF) was calculated.^[37] Figure 4 shows the calculated 3D and projected 2D ELF (iso-surface level of 0.93) of Sb₂Se₃ and BiSbSe₃, respectively. The “mushroom” ELF shape around Sb atoms is a clear indicator of the existence of lone-pair electrons. The lone-pair electrons are mainly located along the a and c axes. The electronic repulsion between the lone-pair electrons and Sb–Se/Bi–Se bonding electrons could lead to strong anharmonicity along the two axes of Sb₂Se₃ and BiSbSe₃, which is similar to those in CuBiS₂^[38] and SnSe.^[39] These structural and electronic features suggest that ionic bond of Bi–Se and covalent bond in Sb–Se.

To further investigate the origin of the low thermal conductivity, we carried out the evaluations on elastic properties through ultrasonic pulse echo measurements for BiSbSe₃ and Sb₂Se₃. It is worth mentioning that it is impossible to extract the directional dependence of the different moduli from measurement of polycrystalline samples, especially for an orthorhombic system. Therefore, the values presented in this work are considered to be directionally averaged estimates.^[40] Then we

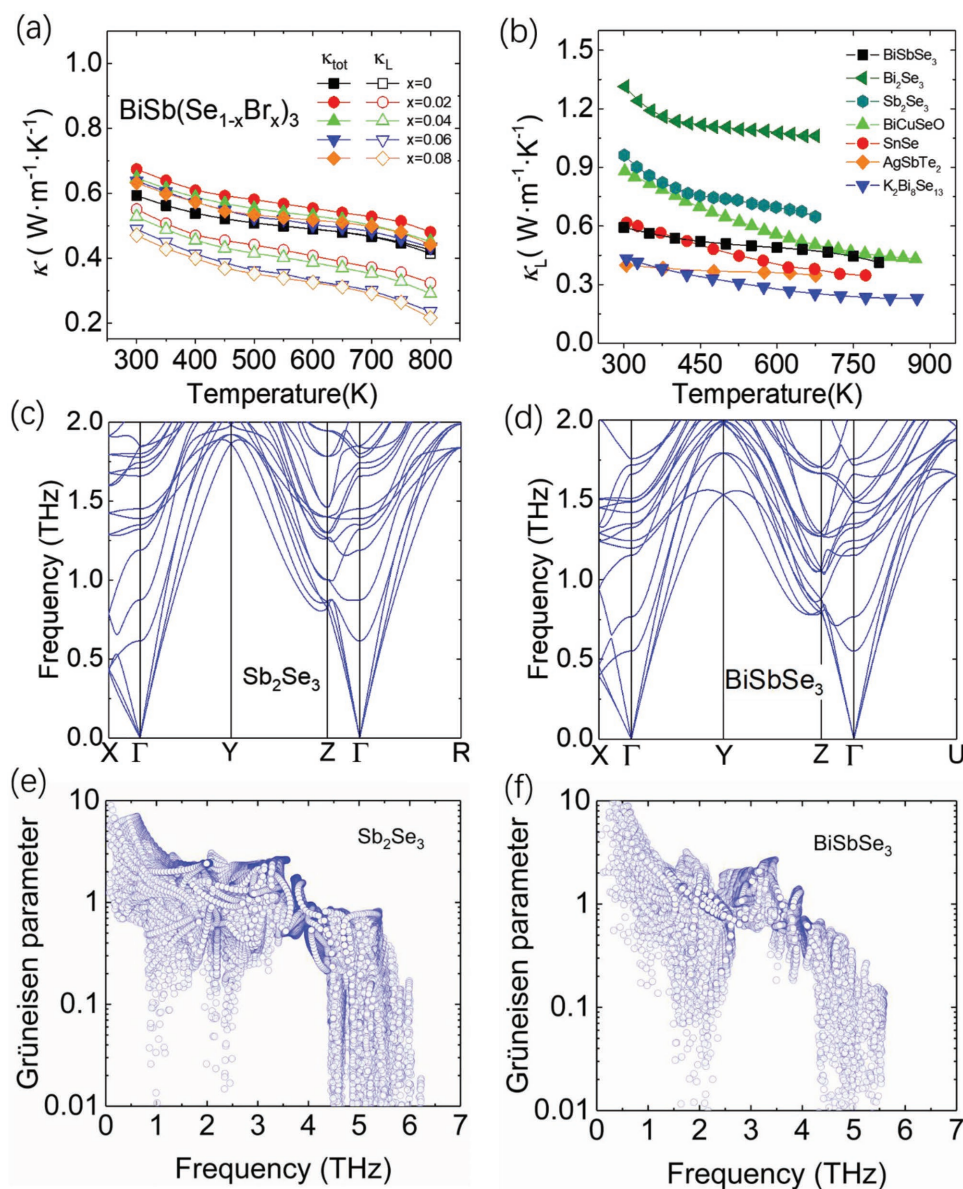


Figure 3. Thermal conductivities as a function of temperature for $\text{BiSb}(\text{Se}_{1-x}\text{Br}_x)_3$ ($x = 0-0.08$): a) total and lattice thermal conductivity, b) lattice thermal conductivity comparisons for BiSbSe_3 and other typical TE materials with low lattice thermal conductivities, Bi_2Se_3 ,^[31] Sb_2Se_3 ,^[31] BiCuSeO ,^[34] SnSe ,^[16] AgSbTe_2 ,^[35] $\text{K}_2\text{Bi}_8\text{Se}_{13}$.^[36] Calculated phonon dispersion and mode Grüneisen parameters for Sb_2Se_3 c,e) and BiSbSe_3 d,f), respectively.

obtained the longitudinal (LA) (v_l) and shear (v_s) phonon velocities, Young's modulus (E), Grüneisen parameter (γ), and Debye temperature (θ_D). As we known, elastic properties are widely used to evaluate the interatomic bonding strength and lattice vibration anharmonicity in a crystal lattice. Usually, a large Grüneisen parameter (γ), a small Debye temperature (θ_D) and Young's modulus (E) result in a low lattice thermal conductivity via the formula as follows:^[34,41,42]

$$\kappa_L = \frac{3.0 \times 10^{-5} \overline{M_a} a \theta_D^3}{T \gamma^2 v^{2/3}} \quad (1)$$

$$\kappa_L \propto \frac{\rho^{1/6} E^{1/2}}{(M/m)^{2/3}} \quad (2)$$

where ρ is the sample density, M_a is the mean atomic weight of all the constituent atoms, a^3 is the average volume occupied by one atom, v is the number of atoms in the unit primitive cell, M is the atomic weight of the molecule of the compound, and m is the number of atoms in the molecule. As shown above, Equations (1) and (2) summarize the key-variable interconnections quite nicely.

In this work, average sound velocity (v_a), Young's modulus (E), shear modulus (G), Poisson ratio ν_p , and Grüneisen parameter (γ) can be calculated from the sound velocity through following relationships:^[34,41,42]

$$v_a = \left[\frac{1}{3} \left(\frac{1}{v_l^3} + \frac{2}{v_s^3} \right) \right]^{-1/3} \quad (3)$$

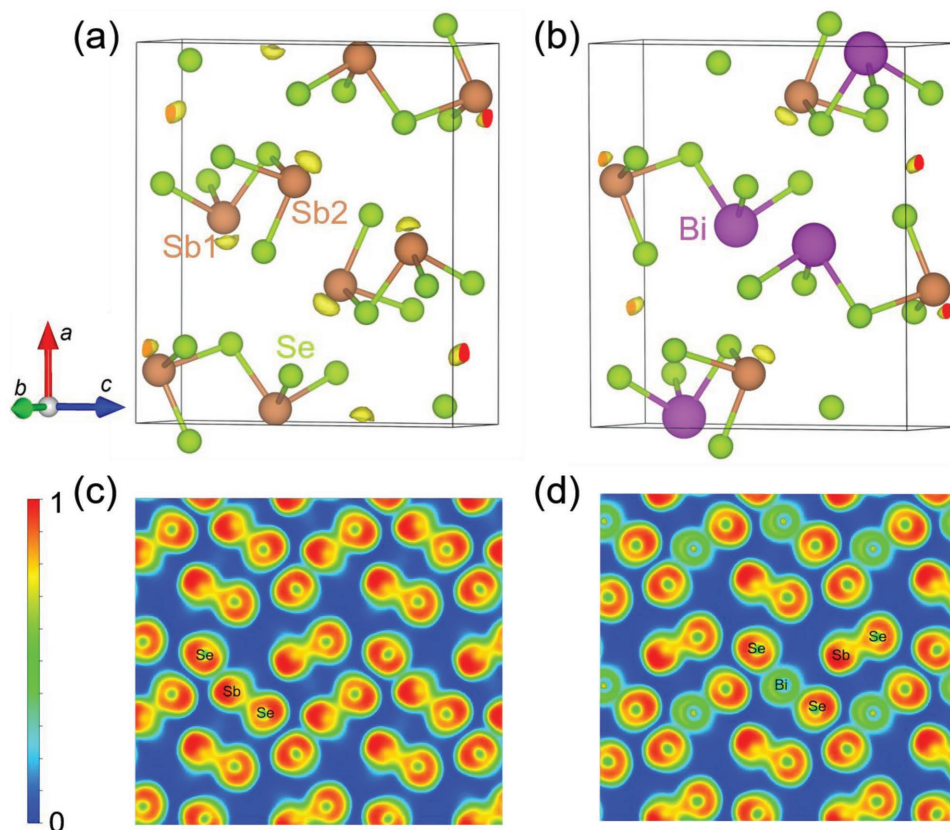


Figure 4. Calculated 3D ELF for a) Sb_2Se_3 and b) BiSbSe_3 . The isosurface level is 0.93. The projected ELF of c) Sb_2Se_3 and d) BiSbSe_3 onto the (010) plane. Larger electron localizations indicate a strong covalent bond and lower anharmonicity.

$$E = \frac{\rho v_s^2 (3v_l^2 - 4v_s^2)}{(v_l^2 - v_s^2)} \quad (4)$$

$$v_p = \frac{1 - 2(v_s/v_l)^2}{2 - 2(v_s/v_l)^2} \quad (5)$$

$$G = \frac{E}{2(1 + v_p)} \quad (6)$$

$$\gamma = \frac{3}{2} \left(\frac{1 + v_p}{2 - 3v_p} \right) \quad (7)$$

where ρ is the sample density, v_p is the Poisson ratio. v_l is the longitudinal phonon velocity and v_s is the shear phonon velocity which can be acquired directly by the ultrasonic pulse echo measurements, as listed in Table 2.

The low lattice thermal conductivity values in BiSbSe_3 system can be partly explained in terms of vibrations of phonon modes. The calculated phonon dispersion is shown in Figure 3c,d. There is no imaginary frequency, indicating the thermodynamic stability of the two structures. It can be seen that Bi doping leads to a soften in the acoustic mode, due to the weak bonding interaction along a and c directions as analyzed above. Bi substitution also leads to a clear mode soften and significant decrease in group velocities, i.e., longitudinal (LA) 2478 m s^{-1}

and transverse (TA) 1008 m s^{-1} and 1014 m s^{-1} velocities for BiSbSe_3 along a axis. The mode Grüneisen parameters, an indicator of anharmonicity, are shown in Figure 3e,f. It can be seen that soft acoustic modes also give rise to larger mode Grüneisen parameters. Near the zone center, Grüneisen parameter is close to 10, larger than that of SnSe .^[16] The physical origin of the large anharmonicity in BiSbSe_3 may be ascribed to the repulsion between the $5s^2$ lone-pair electrons of Sb and $3p$ orbital of Se, similar to other reported strong anharmonicity and low lattice thermal conductivity in SnSe ,^[16] AgSbSe_2 ,^[43] NaSbSe_2 ,^[43] and Ti_3VSe_4 .^[44] Therefore, the combination of very low group velocities and strong anharmonicity governs the low lattice thermal conductivity of BiSbSe_3 .

As shown in Table 2, the average sound velocity (v_a) of BiSbSe_3 ($\approx 1629 \text{ m s}^{-1}$) is much lower than that of Bi_2Se_3 ($\approx 2104 \text{ m s}^{-1}$) and BiCuSeO ($\approx 2107 \text{ m s}^{-1}$). What is more, a small average sound velocity (v_a) leads to a small Young's modulus (E), ($\approx 34.9 \text{ GPa}$) of BiSbSe_3 , which is not only much smaller than that of Bi_2Se_3 ($\approx 70.3 \text{ GPa}$) and BiCuSeO ($\approx 76.5 \text{ GPa}$) but also comparable to those of ultra-low thermal conductivity materials AgSbTe_2 ($\approx 39.2 \text{ GPa}$) and $\text{K}_2\text{Bi}_8\text{Se}_{13}$ ($\approx 37.1 \text{ GPa}$). The Grüneisen parameter (γ) of BiSbSe_3 is (≈ 1.89), which is linked to strong anharmonicity of the crystal structure. As we known, the origin of the low thermal conductivity of SnSe , with a large average Grüneisen parameter (γ) (≈ 3.13), can be attributed to the high degree of lattice anharmonicity partially due to lone-pair electrons of Sn.^[16,43,45–47] Here, BiSbSe_3

Table 2. Comparisons of room-temperature elastic properties of BiSbSe₃ and other thermoelectric materials with low thermal conductivity.

Parameters	BiSbSe ₃	Bi ₂ Se ₃ ^[48]	Sb ₂ Se ₃	BiCuSeO ^[49]	SnSe ^[46]	AgSbTe ₂ ^[45]	K ₂ Bi ₈ Se ₁₃ ^[36]
v_l [m s ⁻¹]	2815	3390	3000	3290	2730	3123	2683
v_s [m s ⁻¹]	1455	1870	1690	1900	1250	1538	1438
v_a [m s ⁻¹]	1629	2083	1882	2107	1420	1727	1605
E [GPa]	34.9	70.3	45.3	76.5	27.7	39.2	37.1
ν_p	0.32	0.28	0.27	0.25	0.44	0.34	0.30
γ	1.89	1.65	1.58	1.50	3.13	2.05	1.77
θ_D [K]	165	205	180	243	142	125	154

shows a large Grüneisen parameter (γ) of (≈ 1.89), which is comparable to AgSbTe₂ (≈ 2.05) and K₂Bi₈Se₁₃ (≈ 1.77),^[36,45] because of the lone-pair electrons of Sb.

Apart from these elastic parameters (sound velocity, Young's modulus, shear modulus, and Grüneisen parameters), the value of Debye temperature could also reflect the thermal conductivity to some extent. Debye temperature θ_D can be estimated as follows:^[41]

$$\theta_D = \frac{h}{k_B} \left[\frac{3N}{4\pi V} \right]^{1/3} v_a \quad (8)$$

where h is Planck's constant, k_B is the Boltzmann constant, N is the number of atoms in a unit cell, V is the unit-cell volume, and v_a is the average phonon velocity, respectively. As listed in Table 2, the Debye temperature (θ_D) of BiSbSe₃ is ≈ 165 K, which is much smaller than that of Bi₂Se₃ (≈ 205 K). It is consistent with the lower lattice thermal conductivity at room temperature (≈ 0.6 W m⁻¹ K⁻¹) of BiSbSe₃ compared to that of Bi₂Se₃ (≈ 1.3 W m⁻¹ K⁻¹), as displayed in Figure 3b.

Because of the intrinsically low thermal conductivity and the effectively optimized power factor, we finally obtain the maximum ZT ~ 1.4 at 800 K for the sample BiSb(Se_{0.94}Br_{0.06})₃ (Figure 5a). Compared to Bi₂Te₃ and Bi₂Se₃, Sb/Se substitutions successfully push the peak of ZT to high temperature. Moreover, ZT of optimized BiSbSe₃ is more competitive than most of the state-of-the-art medium-temperature n -type TE materials, as shown in Figure 5b. In addition, the Figure S7

in the Supporting Information shows that the sample displays an anisotropic behavior since the electrical conductivity and thermal conductivity measured perpendicular to spark plasma sintering (SPS) pressure direction are higher than those parallel to SPS direction. As a result, a higher ZT ~ 1.4 is obtained for the sample perpendicular to SPS direction than ZT ~ 0.8 for the sample parallel to SPS direction.

3. Conclusions

In summary, BiSbSe₃ is a new promising material in the medium-temperature range. It shows extremely low thermal conductivity because of the low elastic properties (phonon velocity $v_a \sim 1629$ m s⁻¹ and Young's modulus $E \sim 34.9$ GPa) and a big Grüneisen parameter γ (≈ 1.89), which are related to the lone-pair electrons of Sb. Additionally, the point defects attributed to solid solution of Br could further reduce the lattice thermal conductivity. Therefore, an ultra-low thermal conductivity (≈ 0.43 W m⁻¹ K⁻¹) at 800 K could be obtained. The Br doping effectively increases the carrier density to a high level of ($\approx 3.7 \times 10^{20}$ cm⁻³), which simultaneously improves the electrical conductivities and the Seebeck coefficients through activating the multiple band conduction. Therefore, the power factor is optimized to ≈ 7.4 μ W cm⁻¹ K⁻² at 800 K. The combination of improved power factor and low thermal conductivity contributes to a high ZT of ≈ 1.4 at 800 K.

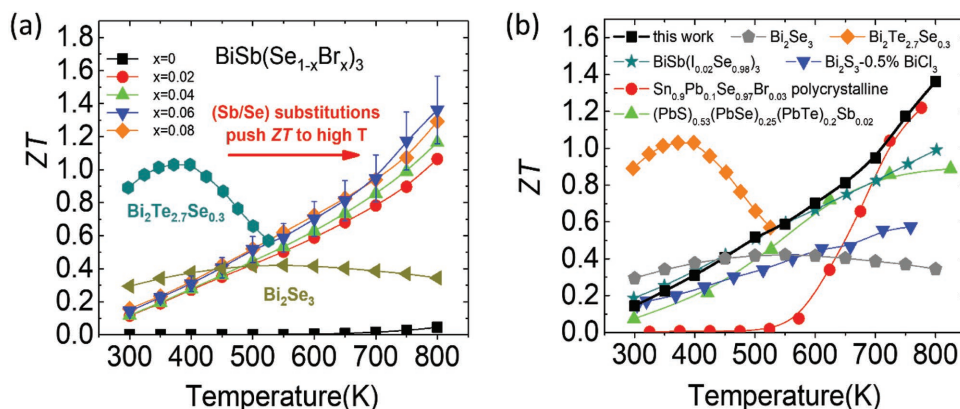


Figure 5. Dimensionless figure of merit ZT values and its comparisons: a) BiSb(Se_{1-x}Br_x)₃ ($x = 0-0.08$), Bi₂Te_{2.7}Se_{0.3},^[24] and Bi₂Se₃; b) ZT comparisons for BiSb(Se_{0.94}Br_{0.06})₃ and other typical medium-temperature n -type TE materials: Bi₂Se₃ (ZT ~ 0.4 at 600 K), Bi₂Te_{2.7}Se_{0.3} (ZT ~ 1.0 at 400 K),^[24] BiSb(I_{0.02}Se_{0.98})₃ (ZT ~ 1.0 at 800 K),^[31] Sn_{0.9}Pb_{0.1}Se_{0.97}Br_{0.03} polycrystalline (ZT ~ 1.2 at 800 K),^[25] (PbS)_{0.53}(PbSe)_{0.25}(PbTe)_{0.2}Sb_{0.02} (ZT ~ 0.9 at 800 K),^[26] Bi₂S₃-0.5%BiCl₃ (ZT ~ 0.6 at 760 K).^[27]

4. Experimental Section

All samples were prepared by melting method followed a subsequent SPS technique. Starting materials were loaded into quartz tubes, which were sealed under a high vacuum (10^{-3} bar), slowly heated up to 1173 K and soaked at 1173 K for 5 h. The tubes were ice quenched to room temperature, and then annealed at 673 K for 48 h. The obtained ingots were ground into powders, and subsequently sintered using SPS. The phases were identified by XRD and the bandgaps were measured by a UV–vis–NIR Spectrophotometer (SHIMADZU UV-3600 Plus). The electrical resistivity and Seebeck coefficient were measured simultaneously in a helium atmosphere at 300–800 K using a Cryoall CTA measurement system. Hall coefficients were measured using a Hall measurement system (Lake Shore 8400 Series, Model 8404). The thermal conductivity was calculated from $\kappa = D \cdot C_p \cdot \rho$, where the thermal diffusivity coefficient (D) was measured using the laser flash diffusivity method in a Netzsch LFA457, the specific heat capacity (C_p) was calculated using Debye model in the range 300–800 K, and the sample density (ρ) was determined using the dimensions and mass of the sample, the sample density was also reconfirmed by gas pycnometer (Micromeritics AccuPyc1340) measurements. STEM and TEM were conducted with a JEOL ARM200F under 200 kV equipped with a cold field emission gun and ASCOR probe corrector. The thin TEM specimens were prepared by conventional methods and include cutting, grinding, dimpling, polishing and Ar-ion milling (Fischione M1051) on a liquid nitrogen cooling stage. The phonon and Grüneisen dispersions were obtained by using first-principles DFT calculations within the quasi-harmonic approximation. More experiment details can be found in Supporting Information.

Supporting Information

Supporting Information is available from the Wiley Online Library or from the author.

Acknowledgements

X.L. and D.W. contributed equally to this work. This work was supported by the National Key Research and Development Program of China under Grant No. 2018YFB0703600, the National Natural Science Foundation of China under Grant No. 51571007, 51632005 and 51772012, the Beijing Municipal Science & Technology Commission under Grant No. Z171100002017002, the Shenzhen Peacock Plan team under Grant No. KQTD2016022619565911, and 111 Project under Grant No. B17002. H.W. and S.P. would like to acknowledge support by the Ministry of Education, Singapore under its Tier 2 Grant (Grant No. MOE2017-T2-1-129). This work was also supported by The High Performance Computing Center of Henan Normal University.

Conflict of Interest

The authors declare no conflict of interest.

Keywords

anharmonicity, BiSbSe₃, low thermal conductivity, multiple conduction bands, thermoelectric

Received: September 16, 2018

Revised: November 5, 2018

Published online: November 26, 2018

- [1] G. J. Tan, L. D. Zhao, M. G. Kanatzidis, *Chem. Rev.* **2016**, *116*, 12123.
- [2] A. J. Minnich, M. S. Dresselhaus, Z. F. Ren, G. Chen, *Energy Environ. Sci.* **2009**, *2*, 466.
- [3] G. J. Snyder, E. S. Toberer, *Nat. Mater.* **2008**, *7*, 105.
- [4] W. G. Zeier, A. Zevkink, Z. M. Gibbs, G. Hautier, M. G. Kanatzidis, G. J. Snyder, *Angew. Chem., Int. Ed.* **2016**, *55*, 6826.
- [5] J. Yang, L. Xi, W. Qiu, L. Wu, X. Shi, L. Chen, J. Yang, W. Zhang, C. Uher, D. J. Singh, *npj Comput. Mater.* **2016**, *2*, 15015.
- [6] M. S. Dresselhaus, G. Chen, M. Y. Tang, R. G. Yang, H. Lee, D. Z. Wang, Z. F. Ren, J. P. Fleurial, P. Gogna, *Adv. Mater.* **2007**, *19*, 1043.
- [7] L. Yang, Z.-G. Chen, M. S. Dargusch, J. Zou, *Adv. Energy Mater.* **2018**, *8*, 1701797.
- [8] L. D. Zhao, H. J. Wu, S. Q. Hao, C. I. Wu, X. Y. Zhou, K. Biswas, J. Q. He, T. P. Hogan, C. Uher, C. Wolverton, V. P. Dravid, M. G. Kanatzidis, *Energy Environ. Sci.* **2013**, *6*, 3346.
- [9] C. Chang, M. H. Wu, D. S. He, Y. L. Pei, C. F. Wu, X. F. Wu, H. L. Yu, F. Y. Zhu, K. D. Wang, Y. Chen, L. Huang, J. F. Li, J. Q. He, L. D. Zhao, *Science* **2018**, *360*, 778.
- [10] Y. Takagiwa, Y. Pei, G. Pomrehn, G. J. Snyder, *Appl. Phys. Lett.* **2012**, *101*, 092102.
- [11] C. M. Jaworski, V. Kulbachinskii, J. P. Heremans, *Phys. Rev. B* **2009**, *80*, 233201.
- [12] J. Q. He, S. N. Girard, J. C. Zheng, L. D. Zhao, M. G. Kanatzidis, V. P. Dravid, *Adv. Mater.* **2012**, *24*, 4440.
- [13] H. Wang, J. L. Wang, X. L. Cao, G. J. Snyder, *J. Mater. Chem. A* **2014**, *2*, 3169.
- [14] Z. G. Chen, G. Han, L. Yang, L. N. Cheng, J. Zou, *Prog. Nat. Sci.: Mater.* **2012**, *22*, 535.
- [15] L. D. Zhao, V. P. Dravid, M. G. Kanatzidis, *Energy Environ. Sci.* **2014**, *7*, 251.
- [16] L. D. Zhao, S. H. Lo, Y. S. Zhang, H. Sun, G. J. Tan, C. Uher, C. Wolverton, V. P. Dravid, M. G. Kanatzidis, *Nature* **2014**, *508*, 373.
- [17] S. N. Girard, T. C. Chasapis, J. Q. He, X. Y. Zhou, E. Hatzikraniotis, C. Uher, K. M. Paraskevopoulos, V. P. Dravid, M. G. Kanatzidis, *Energy Environ. Sci.* **2012**, *5*, 8716.
- [18] D. Wu, L. D. Zhao, S. Q. Hao, Q. K. Jiang, F. S. Zheng, J. W. Doak, H. J. Wu, H. Chi, Y. Gelbstein, C. Uher, C. Wolverton, M. Kanatzidis, J. Q. He, *J. Am. Chem. Soc.* **2014**, *136*, 11412.
- [19] X. F. Tang, W. J. Xie, H. Li, W. Y. Zhao, Q. J. Zhang, M. Niino, *Appl. Phys. Lett.* **2007**, *90*, 012102.
- [20] L. Hu, H. Wu, T. Zhu, C. Fu, J. He, P. Ying, X. Zhao, *Adv. Energy Mater.* **2015**, *5*, 1500411.
- [21] W. S. Liu, K. C. Lukas, K. McEnaney, S. Lee, Q. Zhang, C. P. Opeil, G. Chen, Z. F. Ren, *Energy Environ. Sci.* **2013**, *6*, 552.
- [22] S. Y. Wang, G. J. Tan, W. J. Xie, G. Zheng, H. Li, J. H. Yang, X. F. Tang, *J. Mater. Chem.* **2012**, *22*, 20943.
- [23] W. Zhang, R. Yu, H. J. Zhang, X. Dai, Z. Fang, *New J. Phys.* **2010**, *12*, 065013.
- [24] X. A. Yan, B. Poudel, Y. Ma, W. S. Liu, G. Joshi, H. Wang, Y. C. Lan, D. Z. Wang, G. Chen, Z. F. Ren, *Nano Lett.* **2010**, *10*, 3373.
- [25] C. Chang, Q. Tan, Y. L. Pei, Y. Xiao, X. Zhang, Y. X. Chen, L. Zheng, S. K. Gong, J. F. Li, J. Q. He, L. D. Zhao, *RSC Adv.* **2016**, *6*, 98216.
- [26] M. H. Zhao, C. Chang, Y. Xiao, L. D. Zhao, *J. Alloy Compd.* **2018**, *744*, 769.
- [27] K. Biswas, L. D. Zhao, M. G. Kanatzidis, *Adv. Energy Mater.* **2012**, *2*, 634.
- [28] H. J. Wu, F. S. Zheng, D. Wu, Z. H. Ge, X. Y. Liu, J. Q. He, *Nano Energy* **2015**, *13*, 626.
- [29] Z. Xu, H. Wu, T. Zhu, C. Fu, X. Liu, L. Hu, J. He, J. He, X. Zhao, *NPG Asia Mater.* **2016**, *8*, e302.
- [30] L. D. Zhao, G. J. Tan, S. Q. Hao, J. Q. He, Y. L. Pei, H. Chi, H. Wang, S. K. Gong, H. B. Xu, V. P. Dravid, C. Uher, G. J. Snyder, C. Wolverton, M. G. Kanatzidis, *Science* **2016**, *351*, 141.

- [31] S. Wang, Y. Sun, J. Yang, B. Duan, L. Wu, W. Zhang, J. Yang, *Energy Environ. Sci.* **2016**, 9, 3436.
- [32] Y. M. Zhou, H. J. Wu, Y. L. Pei, C. Chang, Y. Xiao, X. Zhang, S. K. Gong, J. Q. He, L. D. Zhao, *Acta Mater.* **2017**, 125, 542.
- [33] X. Qian, L. Zheng, Y. Xiao, C. Chang, L. D. Zhao, *Inorg. Chem. Front.* **2017**, 4, 719.
- [34] Y. L. Pei, J. Q. He, J. F. Li, F. Li, Q. J. Liu, W. Pan, C. Barreateau, D. Berardan, N. Dragoe, L. D. Zhao, *NPG Asia Mater.* **2013**, 5, e47.
- [35] Y. Amouyal, *Comput. Mater. Sci.* **2013**, 78, 98.
- [36] Y. L. Pei, C. Chang, Z. Wang, M. J. Yin, M. H. Wu, G. J. Tan, H. J. Wu, Y. X. Chen, L. Zheng, S. K. Gong, T. J. Zhu, X. B. Zhao, L. Huang, J. Q. He, M. G. Kanatzidis, L. D. Zhao, *J. Am. Chem. Soc.* **2016**, 138, 16364.
- [37] A. D. Becke, K. E. Edgecombe, *J. Chem. Phys.* **1990**, 92, 5397.
- [38] Z. Z. Feng, T. T. Jia, J. H. Zhang, Y. X. Wang, Y. S. Zhang, *Phys. Rev. B* **2017**, 96, 235205.
- [39] C. Chang, L.-D. Zhao, *Mater. Today Phys.* **2018**, 4, 50.
- [40] J. Y. Cho, X. Shi, J. R. Salvador, G. P. Meisner, J. Yang, H. Wang, A. A. Wereszczak, X. Zhou, C. Uher, *Phys. Rev. B* **2011**, 84, 49.
- [41] K. Kurosaki, A. Kosuga, H. Muta, M. Uno, S. Yamanaka, *Appl. Phys. Lett.* **2005**, 87, 061919.
- [42] C. L. Wan, W. Pan, Q. Xu, Y. X. Qin, J. D. Wang, Z. X. Qu, M. H. Fang, *Phys. Rev. B* **2006**, 74, 144109.
- [43] M. D. Nielsen, V. Ozolins, J. P. Heremans, *Energy Environ. Sci.* **2013**, 6, 570.
- [44] S. Mukhopadhyay, D. S. Parker, B. C. Sales, A. A. Puretzky, M. A. McGuire, L. Lindsay, *Science* **2018**, 360, 1455.
- [45] D. T. Morelli, V. Jovovic, J. P. Heremans, *Phys. Rev. Lett.* **2008**, 101, 035901.
- [46] Y. Xiao, C. Chang, Y. L. Pei, D. Wu, K. L. Peng, X. Y. Zhou, S. K. Gong, J. Q. He, Y. S. Zhang, Z. Zeng, L. D. Zhao, *Phys. Rev. B* **2016**, 94, 125203.
- [47] C. W. Li, J. Hong, A. F. May, D. Bansal, S. Chi, T. Hong, G. Ehlers, O. Delaire, *Nat. Phys.* **2015**, 11, 1063.
- [48] X. Gao, M. Zhou, Y. Cheng, G. F. Ji, *Philos. Mag.* **2016**, 96, 208.
- [49] L. D. Zhao, J. Q. He, D. Berardan, Y. H. Lin, J. F. Li, C. W. Nan, N. Dragoe, *Energy Environ. Sci.* **2014**, 7, 2900.